
LiFT: Lifted Inter-slice Feature Trajectories for 3D Image Generation from 2D Generators

Xinhe Zhang ^{*†}
xinhezhang@g.harvard.edu

Yuyang Zhang ^{*‡}
yuyangzhang@g.harvard.edu

Pengfei Jin [†]
pjini1@mgh.harvard.edu

Arnau Marin-Llobet ^{*}
amarinllobet@seas.harvard.edu

Na Li ^{*}
nali@seas.harvard.edu

Quanzheng Li [†]
li.quanzheng@mgh.harvard.edu

Abstract

High-resolution 3D medical image generation remains challenging because fully volumetric models are computationally expensive, while efficient 2D slice generators often fail to preserve anatomical consistency across the third dimension. We propose LiFT, a framework for Lifted inter-slice Feature Trajectories that factorizes 3D volume synthesis into per-slice image generation and inter-slice trajectory learning. Rather than modeling the volumetric distribution end-to-end, LiFT treats a volume as an ordered trajectory in feature space, capturing how anatomical structures appear, transform, and disappear across depth. A tri-planar drifting loss aligns the trajectory of generated slices with the trajectories of real volumes, enabling distributional learning over inter-slice progressions in unconditional generation; in paired translation, a bidirectional z -context mixer trained against the registered target supplies through-plane coherence while preserving per-slice fidelity. We evaluate LiFT on BraTS 2023 (unconditional and missing-modality MR) and SynthRAD2023 (MR-to-CT). Across these settings, LiFT preserves per-slice quality, approaches the reported cWDM missing-MR reconstruction quality at $\sim 135\times$ lower inference cost (without formal equivalence testing), and improves through-plane coherence on MR-to-CT relative to a no-mapper ablation, demonstrating that lightweight inter-slice trajectory learning is a viable route to high-resolution 3D medical synthesis.

1 Introduction

Medical image synthesis is fundamentally a three-dimensional (3D) problem because the anatomical and pathological targets of interest are volumetric. Tumors, ventricles, edema, white-matter tracts, skull boundaries, air cavities, and bone interfaces are not interpreted as isolated two-dimensional (2D) slices, but through their spatial continuity across a volume. This volumetric structure is also required by many downstream clinical and computational workflows, including segmentation, registration, dose planning, longitudinal monitoring, and image-guided intervention [1]. Generative models for 3D magnetic resonance (MR) and computed tomography (CT) imaging can help address data scarcity and data-sharing constraints [2], support augmentation and benchmarking [3, 4], and enable

^{*}School of Engineering and Applied Sciences, Harvard University

[†]Center for Advanced Medical Computing and Analysis, Massachusetts General Hospital and Harvard Medical School

[‡]Kempner Institute, Harvard University

cross-modality synthesis, such as missing-modality MR completion [5] or MR-to-CT synthesis for MR-only radiotherapy [6].

Existing generative approaches address this volumetric requirement in different ways. Fully 3D generators model inter-slice consistency directly, but often require substantial compromises in memory, resolution, architecture, or training strategy. Prior work has therefore explored hierarchical sub-volume training [7], dense 3D denoising [8, 9], latent-space generation [10, 11], wavelet-domain generation [12, 13], and patch-volume modeling [14]. Despite their differences, these methods share the assumption that volumetric coherence should be learned primarily by a 3D generator. In contrast, slice-wise 2D synthesis can exploit mature high-resolution image-generation backbones and is often more efficient at preserving native in-plane detail. However, independently generated slices do not necessarily form anatomically coherent volumes. Recent two-and-a-half-dimensional [15], adjacent-slice [16], multi-view [17], slice-based latent-diffusion [18], and triplane-aware [19] methods attempt to reduce this gap by injecting limited through-plane context into otherwise slice-oriented synthesis. This line of work suggests that the key challenge is not merely generating realistic slices, but coordinating them across depth.

In many medical synthesis settings, high-resolution in-plane anatomy can be modeled effectively by 2D image-generation architectures. This is partly because clinical MR and CT volumes are often anisotropic, with substantially higher native resolution within each slice than across slices [20, 21], and partly because 2D backbones avoid the memory and optimization burden of fully volumetric generation [22, 23]. However, anatomical structures do not evolve independently from slice to slice. Tumors, edema, ventricles, cortical boundaries, bone interfaces, and air cavities follow continuous spatial trajectories through the volume. As a result, purely slice-wise synthesis can preserve local image detail while still producing unrealistic through-plane discontinuities or inconsistent anatomy [15, 16]. These observations motivate a factorized view of medical volume synthesis, in which high-resolution slice formation and through-plane anatomical organization are treated as related but separable problems.

Motivated by these observations, we propose **LiFT**, a framework for Lifted inter-slice Feature Trajectories in medical volume synthesis. LiFT keeps the core synthesis pathway predominantly 2D while introducing lightweight through-plane modeling to impose volume-level coherence (Fig. 1). The form of volume-level supervision depends on the available data: in the unconditional setting, where no paired target volume exists for each generated sample, LiFT encourages coherence distributionally by matching triplanar trajectories between generated and real volumes; in the paired translation setting with exact target volumes available, LiFT imposes coherence directly through supervised losses and depth-axis context mixing.

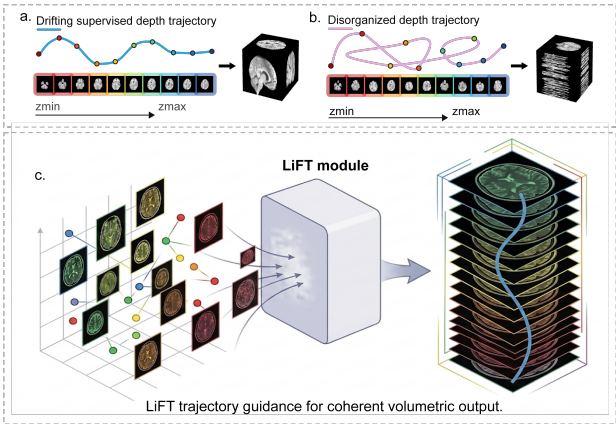


Figure 1: LiFT decouples high-resolution 2D in-plane synthesis from through-plane coherence modeling, adapting supervision to unconditional or paired volume settings.

Contributions. We propose LiFT, a 2D-to-volume synthesis framework for medical image generation and translation. Our main contributions are:

- **Factorized 2D-to-volume synthesis.** LiFT lifts a 2D synthesizer into a volumetric synthesis model using a small learned depth-indexed feature trajectory. The framework adapts its volume-level supervision to the data regime: in the unconditional setting, LiFT-U uses a frozen 2D slice generator and trains a compact depth mapper with tri-planar distributional trajectory matching over completed volumes; in the paired setting, LiFT-C augments a native-resolution 2D translator with a lightweight inter-slice context module over per-slice bottleneck states, enabling direct supervised through-plane context modeling in a single forward pass.

- **Empirical validation across complementary clinical synthesis settings.** We evaluate the same lifting principle across unconditional MR imaging generation, missing-modality MR synthesis, and MR-to-CT synthesis. These experiments assess whether lightweight through-plane organization can improve volume coherence while preserving the resolution and efficiency advantages of 2D synthesis, and compare it with volumetric and slice-wise baselines in terms of image quality, memory usage, inference cost, and through-plane coherence.

2 Related Work

Volumetric and slice-wise medical synthesis. Volumetric methods enforce 3D structure by operating on 3D tensors or compressed 3D representations, including hierarchical sub-volume generative adversarial networks (GANs) [7], 3D and conditional denoising diffusion probabilistic models (DDPMs) [8, 9], latent generative models [10, 11], wavelet-domain models [12, 13], and patch-volume latent diffusion models (LDMs) [14]. These approaches directly model inter-slice dependence, but their volumetric design often requires compromises in memory, spatial resolution, training strategy, or architectural complexity [23]. Slice-wise alternatives instead synthesize volumes by stacking independent 2D outputs from pix2pix-style or CycleGAN-style backbones [24–26, 15], with recent extensions adding adjacent-slice alignment, multi-view averaging, or slice-aggregation modules to recover coherence [16–18]. These methods preserve the efficiency and native in-plane resolution of 2D synthesis, but the resulting volumes can still suffer from discontinuities or inconsistent anatomy across depth [15, 16]. Synthetic CT is a representative application of this tradeoff: SynthRAD2023 benchmarks MR-to-CT and cone-beam-CT-to-CT synthesis under image- and dose-based metrics [27], and patch-based conditional GANs, CycleGANs, U-Nets, and drifting-model variants have all been applied to synthetic-CT generation [28–31]. Across these settings, the remaining challenge is to obtain volumetric coherence without paying the full cost of a fully volumetric generator or relying on independent slice synthesis followed by post hoc consistency correction.

Factorized 2D-to-3D and feature-distribution methods. Closer to LiFT are methods that reduce the cost of volumetric generation by combining 2D and 3D components. Make-A-Volume introduces volumetric layers into a 2D latent diffusion backbone [22], EG3D decouples feature generation from neural rendering through structured three-dimensional-aware representations [32], and TCAM-Diff uses triplane-aware cross-attention diffusion for medical volumes [19]. These methods demonstrate that dense 3D generation is not the only way to obtain volumetric structure. However, they still build 3D awareness into the main generative pathway, either by modifying the backbone, introducing specialized volumetric representations, or coupling synthesis tightly to a 3D rendering or attention mechanism. This leaves a different question open: when a strong 2D synthesizer already produces high-quality in-plane anatomy, can volumetric coherence be added without redesigning the generator itself?

LiFT addresses this question by treating 3D synthesis as a lifting problem rather than a fully 3D generation problem. The main synthesizer remains predominantly 2D and retains most of the representational capacity, while a small depth-indexed feature trajectory module supplies the missing through-plane organization. On the supervisory side, LiFT-U is related to perceptual losses [33], LPIPS [34], feature matching [35], moment-matching kernels [36, 37], and drifting losses [38, 39], which align samples in learned feature spaces rather than requiring pointwise correspondence. Unlike these generic feature-space objectives, LiFT-U applies distributional matching to tri-planar anatomical trajectories of completed volumes, making the supervision explicitly volume-structured. In the paired setting, LiFT-C uses the same lifting principle but replaces distributional trajectory matching with direct supervised depth-axis context modeling. Thus, LiFT differs from prior factorized methods not by introducing another heavy 3D generator, but by isolating the minimum learned through-plane mechanism needed to organize a strong 2D synthesizer into a coherent volume.

3 Problem Formulation

We consider volumetric medical image synthesis settings in which a 3D volume is represented as a stack of 2D slices. This formulation covers both unconditional volume generation and paired image-to-image translation tasks, including missing-modality MRI synthesis and MR-to-CT synthesis.

Let a volume be denoted by $V \in \mathbb{R}^{C \times H \times W \times D}$, where C is the number of image channels or modalities, H and W are the in-plane spatial dimensions, and D indexes the through-plane axis along which 2D slices are stacked. We denote the slice at depth d by $v_d \in \mathbb{R}^{C \times H \times W}$. We study two volumetric synthesis regimes that share this representation but differ in the supervision available to the model.

Unconditional 3D synthesis. Given a target distribution $p_{\text{data}}(V)$ over real volumes, the goal is to generate samples $\hat{V} \sim p_{\text{data}}$. In this setting, each generated volume has no paired ground-truth counterpart. Therefore, whole-volume realism cannot be supervised by a direct voxel-wise comparison to a target volume; instead, it must be encouraged through distributional objectives that compare generated volumes with real volumes.

Paired 3D translation. In contrast, many clinical synthesis tasks provide registered source–target pairs. Given a pair $(X, Y) \in \mathbb{R}^{C_{\text{in}} \times H \times W \times D} \times \mathbb{R}^{C_{\text{out}} \times H \times W \times D}$, the goal is to predict $\hat{Y} \approx Y$ from X . Here, C_{in} denotes the number of input channels or source modalities, such as different contrasts of MR, and C_{out} denotes the number of output channels or target modalities. Both missing-modality MRI synthesis, where the model predicts an unobserved MRI modality from available MRI modalities, and MR-to-CT synthesis, where the model predicts CT from MR, fit this regime. Because the target volume Y is available, direct voxel-level and feature-level supervision can be applied.

In both regimes, a synthesized volume should satisfy two requirements: (i) per-slice anatomical realism, and (ii) through-plane coherence under coronal and sagittal reformats. Our goal is to satisfy both requirements without incurring the memory and compute cost of a fully volumetric generator.

4 Method

LiFT converts a strong 2D synthesizer into a 3D volume generator by separating in-plane synthesis from through-plane organization. The central design is a factorization into two components: a slice synthesizer, which models high-quality 2D anatomy within each slice, and a trajectory module, which coordinates the sequence of slice-level latent or bottleneck codes along the depth axis. This factorization allows us to reuse mature 2D generative or translation models while explicitly learning the missing z -axis structure required for coherent 3D volumes.

We instantiate this idea in two regimes introduced in Section 3. For unconditional 3D synthesis, LiFT-U starts from a frozen 2D slice generator and learns a latent-to-depth trajectory mapper using only unpaired 3D volumes through a tri-planar distributional drifting objective. For paired cross-modal translation, LiFT-C starts from a supervised 2D encoder–decoder and adds a bidirectional z -context mixer over slice bottleneck descriptors, trained with paired reconstruction losses and an explicit through-plane derivative consistency term.

4.1 LiFT-U: distributional lifting for unconditional synthesis

We first focus on the unconditional 3D synthesis setting, where no paired slice-wise supervision is available and the goal is to generate realistic 3D volumes from noise. LiFT-U lifts a pretrained 2D slice generator into a 3D volume generator by learning how its slice-level conditioning codes should evolve with depth. As shown in Figure 2, LiFT-U first freezes a 2D generator trained on axial slices. It then trains a lightweight depth mapper that converts a global latent code and a Fourier-encoded slice coordinate into the per-slice conditioning vector consumed by the frozen generator. The resulting stack of generated slices is supervised not by paired targets, but by a tri-planar distributional drifting loss that compares generated and real slices in axial, coronal, and sagittal feature spaces. We describe these components below.

Frozen 2D slice generator. We first pretrain a 2D generator $G_{2D}(\cdot; \theta)$ to synthesize axial brain MR slices, then freeze θ . The frozen generator maps a per-slice conditioning vector $c_d \in \mathbb{R}^{d_c}$ to a 2D slice,

$$\hat{v}_d = G_{2D}(c_d; \theta). \quad (1)$$

Freezing the slice generator preserves the in-plane anatomical prior and confines all subsequent training to through-plane organization.

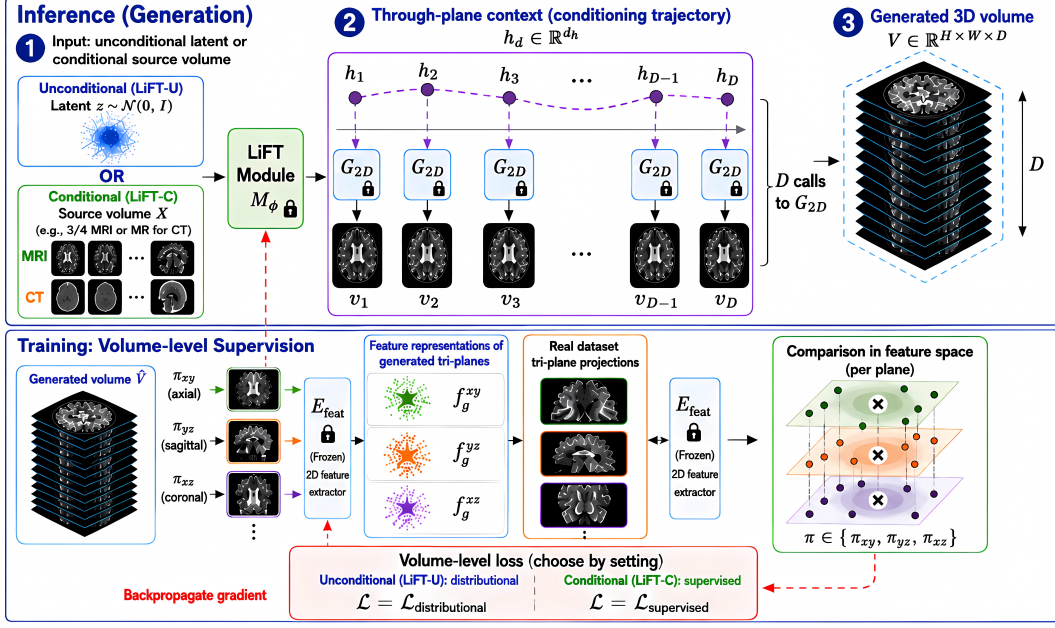


Figure 2: Overview of the LiFT pipeline. A pretrained 2D slice generator is frozen while a depth mapper learns to produce per-slice conditioning vectors from a Fourier-encoded depth coordinate combined with either a global latent code for unconditional generation (LiFT-U) or source-slice features for paired translation (LiFT-C). Generated slices are stacked into a volume and supervised either by a tri-planar drifting loss against axial, coronal, and sagittal feature distributions of real volumes (LiFT-U), or by direct reconstruction against the registered target volume (LiFT-C).

Depth mapper. The trajectory module M_ϕ is a lightweight network that, given a global latent code $z \sim \mathcal{N}(0, I)$ and a Fourier encoding [40] $\gamma(d)$ of the depth coordinate, returns a per-slice conditioning vector,

$$c_d = M_\phi(z, \gamma(d)). \quad (2)$$

The generated volume is

$$\hat{V}(z, \phi) = \text{Stack}_{d=1}^D G_{2D}(M_\phi(z, \gamma(d)); \theta). \quad (3)$$

Only ϕ is trained.

Tri-planar drifting loss. Let $\Pi = \{\pi_{xy}, \pi_{yz}, \pi_{xz}\}$ denote the axial, coronal, and sagittal slicing operators. For each plane $\pi \in \Pi$, let \mathcal{S}_π be its valid slice-index set, and let $E_{\text{feat}} : \mathbb{R}^{H \times W} \rightarrow \mathbb{R}^{d_f}$ be a fixed feature map applied to individual projection slices. For a generated volume \hat{V} and an empirical pool of real volumes $\mathcal{D}_{\text{real}}$, define the real feature bank for plane π as

$$\mathcal{B}_\pi = \{E_{\text{feat}}(\pi_{s'}(V_j)) : V_j \in \mathcal{D}_{\text{real}}, s' \in \mathcal{S}_\pi\}. \quad (4)$$

Given a generated slice feature $g = E_{\text{feat}}(\pi_s(\hat{V}))$, the drifting operator [38] computes a kernel-weighted local target in the corresponding real feature bank and pulls g toward it:

$$\text{Drift}(g, \mathcal{B}_\pi) = \|g - \mu(g; \mathcal{B}_\pi)\|_2^2, \quad \mu(g; \mathcal{B}_\pi) = \frac{\sum_{r \in \mathcal{B}_\pi} K(\|g - r\|/R) r}{\sum_{r \in \mathcal{B}_\pi} K(\|g - r\|/R)}, \quad (5)$$

where K is a Laplacian kernel and R is a fixed bandwidth. The LiFT-U objective averages this drift over generated volumes, projection planes, and slice indices:

$$\mathcal{L}_{\text{LiFT-U}}(\phi) = \frac{1}{|\Pi|} \sum_{\pi \in \Pi} \mathbb{E}_{z \sim \mathcal{N}(0, I), s \sim \text{Unif}(\mathcal{S}_\pi)} [\text{Drift}(E_{\text{feat}}(\pi_s(\hat{V}(z, \phi))), \mathcal{B}_\pi)]. \quad (6)$$

4.2 LiFT-C: supervised lifting for paired translation

We next consider the paired conditional setting, where each source volume X has a registered target volume Y . In this regime, the 2D synthesizer is not a frozen unconditional generator but a supervised encoder–decoder translator. LiFT-C therefore uses the trajectory module differently: instead of mapping random noise and depth to slice generator codes, it reads the sequence of source-slice bottleneck features and produces depth-aware context vectors for target prediction. This allows the model to retain the memory efficiency and strong in-plane modeling of 2D translation while giving each slice access to global through-plane context. LiFT-C is trained with paired reconstruction losses together with a Δ_z -consistency term that directly penalizes discontinuities along the slice axis.

Conditional 2D translator. The 2D synthesizer is an encoder–decoder $G_\theta = D_\theta \circ E_\theta$ applied to source slices $x_d = X_d$. The encoder produces a per-slice latent representation $h_d = E_\theta(x_d)$. In missing-MR synthesis, x_d contains the available MR modalities and the target Y is the missing modality; in MR-to-CT synthesis, x_d contains MR input channels and Y is the CT target.

Bidirectional z -context mixer. A slice-wise translator predicts each target slice independently and therefore cannot directly enforce consistency across neighboring slices or reason over the full depth-wise trajectory. To introduce volume-level context, we first pool each encoder bottleneck feature h_d into a slice descriptor $b_d = \text{Pool}(h_d)$ using spatial global average pooling. The trajectory module M_{ϕ_C} is implemented as a bidirectional GRU [41] over the sequence $b_{1:D}$, augmented with Fourier depth encodings,

$$(c_1, \dots, c_D) = M_{\phi_C}(b_{1:D}, \gamma(1:D)), \quad (7)$$

producing a per-slice context vector c_d that is injected into the decoder bottleneck. The predicted target slice and volume are

$$\hat{y}_d = D_\theta(h_d, c_d), \quad \hat{Y} = \text{Stack}_{d=1}^D \hat{y}_d. \quad (8)$$

Paired supervised objective. Because the registered target Y is available, LiFT-C is trained with direct supervised losses rather than distributional drifting:

$$\mathcal{L}_{\text{LiFT-C}} = \lambda_p \mathcal{L}_{\text{pixel}}(\hat{Y}, Y) + \lambda_s \mathcal{L}_{\text{similarity}}(\hat{Y}, Y) + \lambda_z \mathcal{L}_{\text{spatial}}(\hat{Y}, Y), \quad (9)$$

where $\mathcal{L}_{\text{pixel}}$ is a voxel-wise reconstruction term (e.g., L_1 or Charbonnier), $\mathcal{L}_{\text{similarity}}$ is a structural-similarity or residual-magnitude regularization term (e.g., $1 - \text{MS-SSIM}$ [42]), and $\mathcal{L}_{\text{spatial}}$ is a spatial-derivative consistency term that penalizes through-plane (e.g., $\|\Delta_z \hat{Y} - \Delta_z Y\|_1$) or full spatial-gradient mismatch. The spatial term explicitly penalizes derivative mismatch and complements the learned z -context. Per-task instantiations are described in Sections 5.2 and 5.3. The two-pass native-resolution inference procedure is summarized in Algorithm 2 (Appendix G).

5 Experiments

We evaluate LiFT on three 3D medical synthesis tasks that test whether a 2D synthesizer with a lightweight trajectory or context module can recover useful volumetric structure. Tasks A and B use BraTS 2023 GLI [43–48] for unconditional 3D brain MR generation and missing-modality MR synthesis, respectively. Task C uses SynthRAD2023 [27] for MR-to-CT synthesis.

All models and reproduced baselines are trained and evaluated on a single NVIDIA RTX 5090 GPU. Per-task hyperparameters, preprocessing details, and dataset/model licenses are provided in Appendices F and E.

5.1 Task A: unconditional brain MR generation

Task A evaluates LiFT-U on unconditional 3D brain MR synthesis using the BraTS 2023 GLI cohort. The model generates T1n volumes at $128 \times 128 \times 128$ resolution. Following the WDM evaluation setting [12], volumes are skull-stripped, intensity-normalized to $[-1, 1]$, and resampled to an isotropic 128^3 grid.

We instantiate LiFT-U as described in Section 4: an axial 2D slice generator is trained first and then frozen while a lightweight depth mapper organizes generated slices into coherent volumes. For this

task, the depth mapper has 1.455M trainable parameters, and the tri-planar drift loss uses features from a frozen ImageNet-pretrained ResNet-18. Optimizer, learning rate, and batch construction are summarized in Appendix F.

We evaluate volume-distribution quality under the WDM protocol [12]. Fréchet Inception Distance (FID) is computed using 2048-dimensional MedicalNet ResNet-50 features [49] from 1,000 generated and 1,000 real volumes. We also report mean MS-SSIM as a diversity proxy and peak GPU memory for synthesizing one 128^3 volume. Baseline values are taken from the WDM evaluation report [12].

LiFT-U obtains the lowest reported FID in Table 1, improving over WDM from 0.154 to 0.066, while reducing inference memory from 2.55 GB to 0.41 GB. Its MS-SSIM is also lower than the volumetric diffusion and GAN baselines, indicating higher sample diversity under this proxy.

Table 1: BraTS GLI unconditional 3D volume generation at 128^3 . Lower is better for all three metrics. FID values are pre-multiplied by 10^3 following the WDM evaluation report [12].

Method	FID $\times 10^3$ ↓	MS-SSIM ↓	Inference mem. (GB) ↓
2.5D LDM	81.06	0.579	6.81
3D DDPM	1.402	0.876	6.51
3D LDM	1.394	0.926	9.82
HA-GAN	0.785	0.905	2.58
WDM (WavU-Net)	0.259	0.879	2.65
WDM	0.154	0.888	2.55
LiFT-U	0.066	0.543	0.41

5.2 Task B: missing-modality MR synthesis

Task B evaluates LiFT-C on missing-modality MR synthesis using the BraTS 2023 GLI cohort under the cWDM protocol [13]. Given any three of the four contrasts T1n, T1c, T2w, and T2f, the model synthesizes the fourth at native $240 \times 240 \times 155$ resolution. Volumes are clipped to the 0.1–99.9 percentile and normalized to $[0, 1]$; predictions are clipped from $[-1, 1]$ back to $[0, 1]$ and zeroed outside the brain mask (where the target is zero).

We instantiate LiFT-C as described in Section 4.2: the conditional translator is a 2D U-Net with the three available source modalities channel-concatenated as input, while a bidirectional GRU consumes the pooled bottleneck features over all 155 slices and injects a per-slice context vector back at the bottleneck. The model is trained with the LiFT-C objective in Eq. (9), instantiated with L_1 as the pixel term, $1 - \text{MS-SSIM}$ as the similarity term, and $\|\Delta_z \hat{Y} - \Delta_z Y\|_1$ as the spatial term; optimizer, learning rates, and batch construction for Tasks B and C are summarized in Appendix F.

Evaluation uses the BraTS 2023 GLI cohort 219-subject validation split. We report per-contrast 3D PSNR and 3D-Gaussian SSIM, plane-wise SSIM and adjacent-slice derivative error, and per-volume inference time. cWDM values are reported as the published aggregate under the original cWDM protocol [13]; pix2pix and LiFT-C are evaluated under our shared pipeline. Full per-contrast statistics are reported in Appendix C.

Table 2 reports per-contrast PSNR/SSIM and per-volume inference time. LiFT-C generates a native-resolution volume with deterministic non-iterative inference (the two-pass encode/decode procedure in Algorithm 2), requiring only 1.16 s per volume compared with 156.4 s for the 1000-step cWDM sampler measured on the same RTX 5090 hardware and protocol (a $\sim 135\times$ ratio specific to this setup; absolute speedups will vary across hardware). In the ablation study, removing the BiGRU mapper decreases PSNR by 1.42 dB on T2f, the largest degradation among the evaluated contrasts.

5.3 Task C: MR-to-CT synthesis

Task C evaluates LiFT-C on paired MR-to-CT synthesis using SynthRAD2023 Task 1 Brain [27]. We use an internal patient-level 80/20 split of the 180 subjects, yielding 144 training and 36 test cases. A fixed subset of the 144 training cases is held out as an internal validation fold for checkpoint selection; the 36 test cases are used only for final evaluation. The input is a T1-weighted MR volume

Table 2: Missing-MR synthesis on BraTS 2023 GLI ($N = 219$ validation) under the cWDM protocol [13]. Each contrast cell reports PSNR \uparrow / SSIM \uparrow .

Method	T1n	T1c	T2w	T2f	Inference Time (s)
pix2pix	27.61 / 0.9475	25.91 / 0.9316	26.69 / 0.9419	25.19 / 0.9169	0.05
cWDM	29.74 / 0.9622	27.32 / 0.9451	28.81 / 0.9588	27.83 / 0.9438	156.40
LiFT-C, no mapper	28.97 / 0.9608	27.30 / 0.9455	28.40 / 0.9567	26.46 / 0.9393	—
LiFT-C	29.42 / 0.9615	27.40 / 0.9460	28.53 / 0.9571	27.88 / 0.9424	1.16

and the target is the registered CT. Following the preprocessing pipeline used for the CBAM3D-UNet baseline [50], MR volumes are z-score-normalized over the full volume, CT volumes are clipped to $[-1000, 2000]$ HU and scaled to $[-1, 1]$, and both modalities are cropped to 128^3 using the SynthRAD brain-mask bounding-box center.

We instantiate LiFT-C as a residual two-stage variant of the framework described in Section 4.2. Stage 1 is a frozen axial 2D translator that predicts a baseline CT. Stage 2 applies a BiGRU z -context mixer and predicts an additive correction δ_z , trained with the LiFT-C objective in Eq. (9) instantiated with a Charbonnier pixel term, a residual-magnitude regularization on δ_z as the similarity term, and a spatial-gradient L_1 as the spatial term. The *LiFT-C, no mapper* baseline corresponds to Stage 1 alone.

We report full-volume MAE in Hounsfield units, PSNR, SSIM, and NCC, together with region-specific MAE for soft tissue, bone, air, and bone \cup air boundary regions, following clinical sCT evaluation practice that stratifies image-similarity by HU-defined tissue type [27, 51]. Region-mask construction details and the clinical motivation for these tissue strata are given in Appendix B. Baselines, run by us on the same split, are a 3D CBAM-attention U-Net (CBAM3D-UNet) [50] reimplemented from the published architecture description (no public code), and axial 2D pix2pix-U-Net and pix2pix-ResNet.

Table 3 reports MR-to-CT results on the 36-subject test split. LiFT-C obtains 57.50 HU MAE, 28.49 dB PSNR, 0.8740 SSIM, and 0.9200 NCC, the lowest MAE and highest PSNR, SSIM, and NCC among the evaluated methods; the gap over the no-mapper Stage 1 baseline is small in voxel-wise MAE. Table 4 reports through-plane coherence: LiFT-C has the lowest full-volume and bone Δ_z MAE and the highest Δ_z correlation. Compared with the no-mapper baseline, adding the BiGRU reduces full-volume Δ_z MAE from 42.73 to 38.41 and increases Δ_z correlation from 0.675 to 0.729, indicating that the trajectory module contributes primarily to inter-slice consistency rather than to in-plane accuracy. Paired Wilcoxon tests for LiFT-C versus the no-mapper baseline are summarized in Appendix C.

Table 3: MR-to-CT synthesis on SynthRAD2023 [27] ($n = 36$ test). MAE in HU. Values are mean \pm std; paired ablation statistics are summarized in Appendix C.

Method	MAE \downarrow	PSNR \uparrow	SSIM \uparrow	NCC \uparrow
Pix2pix-UNet	78.38 \pm 11.92	26.41 \pm 1.06	0.8082 \pm 0.0374	0.8700 \pm 0.0422
Pix2pix-ResNet	59.30 \pm 9.90	28.43 \pm 1.18	0.8637 \pm 0.0276	0.9172 \pm 0.0295
CBAM3D-UNet	64.52 \pm 9.47	27.82 \pm 1.14	0.8500 \pm 0.0266	0.9073 \pm 0.0316
LiFT-C, no mapper	59.40 \pm 9.49	28.31 \pm 1.26	0.8679 \pm 0.0261	0.9163 \pm 0.0270
LiFT-C	57.50 \pm 9.55	28.49 \pm 1.33	0.8740 \pm 0.0260	0.9200 \pm 0.0260

Table 4: Through-plane coherence on MR-to-CT ($n = 36$ test). Δ_z denotes adjacent-slice differences along z . Bold marks the best (lowest for \downarrow , highest for \uparrow) per column.

Method	Δ_z MAE Full \downarrow	Δ_z MAE Bone \downarrow	Δ_z MAE Air \downarrow	Δ_z corr \uparrow
Pix2pix-UNet	52.20	180.23	199.71	0.575
Pix2pix-ResNet	44.91	159.54	186.91	0.650
CBAM3D-UNet	39.88	141.10	142.37	0.713
LiFT-C, no mapper	42.73	151.73	172.21	0.675
LiFT-C	38.41	135.52	151.28	0.729

6 Limitations

LiFT is designed to add through-plane organization to an existing 2D synthesizer, rather than to replace the in-plane synthesis model. Its performance therefore remains coupled to the quality of the slice generator or translator. In-plane errors such as hallucinated anatomy, missing structures, poor contrast recovery, or degraded bone/air interfaces are outside the primary scope of the trajectory module. This is most visible in MR-to-CT, where the residual LiFT-C stage improves global and through-plane metrics but leaves substantial residual error in high-HU and low-HU regions such as bone and air.

The two LiFT instantiations also differ in their supervision assumptions. LiFT-U uses distributional trajectory matching, so its guarantees are distributional rather than instance-specific; evaluation is correspondingly based on image-quality metrics and qualitative reformat. LiFT-C uses direct volumetric supervision, but assumes paired and accurately registered source-target volumes. Mis-registration, missing anatomy, or systematic preprocessing errors may therefore be absorbed by the learned correction.

Our evaluation focuses on brain imaging benchmarks: brain MR generation, brain missing-modality MR synthesis, and brain MR-to-CT synthesis. It does not establish performance on thoracic, abdominal, pelvic, or otherwise highly deformable anatomy, nor under multi-institutional domain shift, scanner or protocol variation, or pathology distributions outside the benchmark cohorts. The MR-to-CT study reports image-domain metrics, including MAE, PSNR, SSIM, NCC, and through-plane derivative consistency; dose error, contouring impact, registration robustness, reader preference, and other task-level clinical endpoints remain outside the present study. Similarly, the missing-MR comparison uses published cWDM aggregate values, which precludes formal paired statistical testing against cWDM.

Broader impact and safety. Synthetic medical images may reproduce dataset biases, obscure acquisition-specific artifacts, or be misused as fabricated clinical evidence. Generative models may also leak training information if they memorize individual subjects. We therefore restrict this work to benchmark evaluation and make no claim of clinical deployability. As a preliminary privacy check, we conduct nearest-neighbor retrieval probes for all three tasks (Appendix D) and find no evidence of exact copying relative to held-out real-volume baselines. These probes are not a substitute for comprehensive privacy, bias, and governance analyses, which would be required before clinical or data-sharing use.

7 Conclusion

LiFT studies a simple alternative to fully volumetric medical synthesis: keep the main generator slice-based, and learn only the missing through-plane organization. In the unconditional setting, this takes the form of a depth-indexed trajectory mapper trained with tri-planar distributional matching. In paired translation, it becomes a bidirectional z -context module trained with direct volumetric supervision.

Across unconditional MR generation, missing-modality MR synthesis, and MR-to-CT translation, this factorization retains the computational profile of 2D synthesis while improving volume-level coherence. LiFT-U reports the lowest FID in this protocol-matched comparison while using less inference memory than the volumetric baselines under the WDM-style protocol. LiFT-C approaches the reported cWDM missing-MR reconstruction quality at $\sim 135\times$ lower inference cost, and on MR-to-CT the gains are larger in Δ_z -based metrics than in voxel-wise MAE. This pattern is consistent with the central hypothesis of the paper: much of the missing value in slice-wise synthesis is not additional in-plane capacity, but explicit organization of how anatomy evolves across depth.

LiFT should therefore be viewed as a lightweight volumetric coordination mechanism complementary to stronger in-plane generators, fully volumetric models, and clinical validation. It is most relevant when high-resolution 2D synthesis is already effective and the remaining bottleneck is inter-slice consistency. Future work should test this principle under external domain shift, clinical downstream endpoints, and task-specific safety constraints.

References

- [1] Kalina Chupetlovska, Tugba Akinci D’Antonoli, Zuhir Bodalal, Mohamed A. Abdelatty, Hendrik Erenstein, João Santinha, Merel Huisman, Jacob J. Visser, Stefano Trebeschi, and Kevin B. W. Groot Lipman. ESR essentials: a step-by-step guide of segmentation for radiologists—practice recommendations by the European Society of Medical Imaging Informatics. *European Radiology*, 35(11):6894–6904, 2025. doi: 10.1007/s00330-025-11621-1.
- [2] Hoo-Chang Shin, Neil A. Tenenholtz, Jameson K. Rogers, Christopher G. Schwarz, Matthew L. Senjem, Jeffrey L. Gunter, Katherine P. Andriole, and Mark Michalski. Medical image synthesis for data augmentation and anonymization using generative adversarial networks. In *Simulation and Synthesis in Medical Imaging (SASHIMI), MICCAI Workshop*, pages 1–11. Springer International Publishing, 2018. doi: 10.1007/978-3-030-00536-8_1.
- [3] Maayan Frid-Adar, Idit Diamant, Eyal Klang, Michal Amitai, Jacob Goldberger, and Hayit Greenspan. GAN-based synthetic medical image augmentation for increased CNN performance in liver lesion classification. *Neurocomputing*, 321:321–331, 2018. doi: 10.1016/j.neucom.2018.09.013.
- [4] Mahmoud Ibrahim, Yasmina Al Khalil, Sina Amirrajab, Chang Sun, Marcel Breeuwer, Josien Pluim, Bart Elen, Gokhan Ertaylan, and Michel Dumontier. Generative AI for synthetic data across multiple medical modalities: A systematic review of recent developments and challenges. *arXiv preprint arXiv:2407.00116*, 2024. URL <https://arxiv.org/abs/2407.00116>.
- [5] Richard Acs and Hanqi Zhuang. A review on cross-contrast MRI image synthesis through deep learning. *Discover Imaging*, 2(1), 2025. doi: 10.1007/s44352-025-00012-3.
- [6] Junghyun Roh, Dongmin Ryu, and Jimin Lee. CT synthesis with deep learning for MR-only radiotherapy planning: a review. *Biomedical Engineering Letters*, 14(6):1259–1278, 2024. doi: 10.1007/s13534-024-00430-y.
- [7] Li Sun, Junxiang Chen, Yanwu Xu, Mingming Gong, Ke Yu, and Kayhan Batmanghelich. Hierarchical amortized GAN for 3d high resolution medical image synthesis. *IEEE Journal of Biomedical and Health Informatics*, 26(8):3966–3975, 2022. doi: 10.1109/JBHI.2022.3172976.
- [8] Firas Khader, Gustav Mueller-Franzes, Soroosh Tayebi Arasteh, Tianyu Han, Christoph Haarbuerger, Maximilian Schulze-Hagen, Philipp Schad, Sandy Engelhardt, Bettina Baessler, Sebastian Foersch, Johannes Stegmaier, Christiane Kuhl, Sven Nebelung, Jakob Nikolas Kather, and Daniel Truhn. Denoising diffusion probabilistic models for 3D medical image generation. *Scientific Reports*, 13(1):7303, 2023. doi: 10.1038/s41598-023-34341-2.
- [9] Zolnamar Dorjsembe, Hsing-Kuo Pao, Sodtavilan Odonchimed, and Furen Xiao. Conditional diffusion models for semantic 3D brain MRI synthesis. *IEEE Journal of Biomedical and Health Informatics*, 28(7):4084–4093, 2024. doi: 10.1109/JBHI.2024.3385504.
- [10] Walter H. L. Pinaya, Petru-Daniel Tudosiu, Jessica Dafflon, Pedro F. da Costa, Virginia Fernandez, Parashkev Nachev, Sebastien Ourselin, and M. Jorge Cardoso. Brain imaging generation with latent diffusion models. In *Deep Generative Models (DGM4MICCAI 2022), Lecture Notes in Computer Science*, volume 13609, pages 117–126. Springer, 2022. doi: 10.1007/978-3-031-18576-2_12.
- [11] Jonghun Kim and Hyunjin Park. Adaptive latent diffusion model for 3D medical image to image translation: Multi-modal magnetic resonance imaging study. In *Proceedings of the IEEE/CVF Winter Conference on Applications of Computer Vision (WACV)*, pages 7604–7613, 2024. doi: 10.1109/WACV57701.2024.00743.
- [12] Paul Friedrich, Julia Wolleb, Florentin Bieder, Alicia Durrer, and Philippe C. Cattin. *WDM: 3D Wavelet Diffusion Models for High-Resolution Medical Image Synthesis*, page 11–21. Springer Nature Switzerland, October 2024. ISBN 9783031727443. doi: 10.1007/978-3-031-72744-3_2. URL http://dx.doi.org/10.1007/978-3-031-72744-3_2.
- [13] Paul Friedrich, Alicia Durrer, Julia Wolleb, and Philippe C. Cattin. cWDM: Conditional wavelet diffusion models for cross-modality 3d medical image synthesis, 2024.

- [14] Haoshen Wang, Zhentao Liu, Kaicong Sun, Xiaodong Wang, Dinggang Shen, and Zhiming Cui. 3D MedDiffusion: A 3D medical latent diffusion model for controllable and high-quality medical image generation, 2024. URL <https://arxiv.org/abs/2412.13059>.
- [15] Bin Sun, Shuangfu Jia, Xiling Jiang, and Fucang Jia. Double U-Net CycleGAN for 3D MR to CT image synthesis. *International Journal of Computer Assisted Radiology and Surgery*, 18(1): 149–156, 2023. doi: 10.1007/s11548-022-02732-x.
- [16] Kyobin Choo, Youngjun Jun, Mijin Yun, and Seong Jae Hwang. Slice-consistent 3D volumetric brain CT-to-MRI translation with 2D brownian bridge diffusion model. In *Medical Image Computing and Computer Assisted Intervention – MICCAI 2024*, volume 15007 of *Lecture Notes in Computer Science*, pages 657–667. Springer, 2024. doi: 10.1007/978-3-031-72104-5_63.
- [17] Tianqi Chen, Jun Hou, Yinchu Zhou, Huidong Xie, Xiongchao Chen, Qiong Liu, Xueqi Guo, Menghua Xia, James S. Duncan, Chi Liu, and Bo Zhou. 2.5D multi-view averaging diffusion model for 3D medical image translation: Application to low-count PET reconstruction with CT-less attenuation correction, 2024. URL <https://arxiv.org/abs/2406.08374>.
- [18] Aghiles Kebaili, Jérôme Lapuyade-Lahorgue, Pierre Vera, and Su Ruan. 3D MRI synthesis with slice-based latent diffusion models: Improving tumor segmentation tasks in data-scarce regimes. In *2024 IEEE International Symposium on Biomedical Imaging (ISBI)*. IEEE, 2024. doi: 10.1109/ISBI56570.2024.10635533.
- [19] Zhenkai Zhang, Krista A. Ehinger, and Tom Drummond. TCAM-Diff: Triplane-aware cross-attention medical diffusion model. *Proceedings of the AAAI Conference on Artificial Intelligence*, 39(21):22732–22740, 2025. doi: 10.1609/aaai.v39i21.34433.
- [20] Cheng Peng, Wei-An Lin, Haofu Liao, Rama Chellappa, and S. Kevin Zhou. SAINT: Spatially aware interpolation NeTwork for medical slice synthesis. In *Proceedings of the IEEE/CVF Conference on Computer Vision and Pattern Recognition (CVPR)*, pages 7747–7756. IEEE, 2020. doi: 10.1109/CVPR42600.2020.00777.
- [21] Alex Ling Yu Hung, Haoxin Zheng, Kai Zhao, Xiaoxi Du, Kaifeng Pang, Qi Miao, Steven S. Raman, Demetri Terzopoulos, and Kyunghyun Sung. CSAM: A 2.5D cross-slice attention module for anisotropic volumetric medical image segmentation. In *Proceedings of the IEEE/CVF Winter Conference on Applications of Computer Vision (WACV)*, pages 5911–5920. IEEE, 2024. doi: 10.1109/WACV57701.2024.00582.
- [22] Lingting Zhu, Zeyue Xue, Zhenchao Jin, Xian Liu, Jingzhen He, Ziwei Liu, and Lequan Yu. Make-a-volume: Leveraging latent diffusion models for cross-modality 3D brain MRI synthesis. In *Medical Image Computing and Computer Assisted Intervention – MICCAI 2023*, volume 14229 of *Lecture Notes in Computer Science*, pages 592–601. Springer, 2023. doi: 10.1007/978-3-031-43999-5_56.
- [23] Florentin Bieder, Julia Wolleb, Alicia Durrer, Robin Sandkühler, and Philippe C. Cattin. Memory-efficient 3D denoising diffusion models for medical image processing. In *Proceedings of Medical Imaging with Deep Learning (MIDL)*, volume 227 of *Proceedings of Machine Learning Research*, pages 552–567. PMLR, 2024. URL <https://proceedings.mlr.press/v227/bieder24a.html>.
- [24] Phillip Isola, Jun-Yan Zhu, Tinghui Zhou, and Alexei A. Efros. Image-to-image translation with conditional adversarial networks. In *Proceedings of the IEEE Conference on Computer Vision and Pattern Recognition (CVPR)*, pages 5967–5976, 2017. doi: 10.1109/CVPR.2017.632.
- [25] Jun-Yan Zhu, Taesung Park, Phillip Isola, and Alexei A. Efros. Unpaired image-to-image translation using cycle-consistent adversarial networks. In *Proceedings of the IEEE International Conference on Computer Vision (ICCV)*, pages 2242–2251, 2017. doi: 10.1109/ICCV.2017.244.
- [26] Minh Hieu Phan, Zhibin Liao, Johan W. Verjans, and Minh-Son To. Structure-preserving synthesis: MaskGAN for unpaired MR-CT translation. In *Medical Image Computing and Computer Assisted Intervention – MICCAI 2023*, volume 14229 of *Lecture Notes in Computer Science*, pages 56–65. Springer, 2023. doi: 10.1007/978-3-031-43999-5_6.

- [27] Evi M. C. Huijben et al. Generating synthetic computed tomography for radiotherapy: SynthRAD2023 challenge report. *Medical Image Analysis*, 97:103276, 2024. doi: 10.1016/j.media.2024.103276.
- [28] Peter Klages, Ilyes Benslimane, Sadegh Riyahi, Jue Jiang, Margie Hunt, Joseph O. Deasy, Harini Veeraraghavan, and Neelam Tyagi. Patch-based generative adversarial neural network models for head and neck MR-only planning. *Medical Physics*, 47(2):626–642, 2020. doi: 10.1002/mp.13927.
- [29] Seung Kwan Kang, Hyun Joon An, Hyeongmin Jin, Jung-in Kim, Eui Kyu Chie, Jong Min Park, and Jae Sung Lee. Synthetic CT generation from weakly paired MR images using cycle-consistent GAN for MR-guided radiotherapy. *Biomedical Engineering Letters*, 11(3):263–271, 2021. doi: 10.1007/s13534-021-00195-8.
- [30] Reza Farjam, Himanshu Nagar, Xi Kathy Zhou, David Ouellette, Silvia Chiara Formenti, and J. Keith DeWynngaert. Deep learning-based synthetic CT generation for MR-only radiotherapy of prostate cancer patients with 0.35t MRI linear accelerator. *Journal of Applied Clinical Medical Physics*, 22(8):93–104, 2021. doi: 10.1002/acm2.13327.
- [31] Qing Lyu, Jianxu Wang, Jeremy Hudson, Ge Wang, and Christopher T. Whitlow. MRI-to-CT synthesis using drifting models. *arXiv preprint arXiv:2603.28498*, 2026. URL <https://arxiv.org/abs/2603.28498>.
- [32] Eric R. Chan, Connor Z. Lin, Matthew A. Chan, Koki Nagano, Boxiao Pan, Shalini De Mello, Orazio Gallo, Leonidas Guibas, Jonathan Tremblay, Sameh Khamis, Tero Karras, and Gordon Wetzstein. Efficient geometry-aware 3D generative adversarial networks. In *Proceedings of the IEEE/CVF Conference on Computer Vision and Pattern Recognition (CVPR)*, pages 16123–16133, 2022. doi: 10.1109/CVPR52688.2022.01565.
- [33] Justin Johnson, Alexandre Alahi, and Li Fei-Fei. Perceptual losses for real-time style transfer and super-resolution. In *European Conference on Computer Vision (ECCV)*, volume 9906 of *Lecture Notes in Computer Science*, pages 694–711. Springer, 2016. doi: 10.1007/978-3-319-46475-6_43.
- [34] Richard Zhang, Phillip Isola, Alexei A. Efros, Eli Shechtman, and Oliver Wang. The unreasonable effectiveness of deep features as a perceptual metric. In *Proceedings of the IEEE Conference on Computer Vision and Pattern Recognition (CVPR)*, pages 586–595, 2018. doi: 10.1109/CVPR.2018.00068.
- [35] Tim Salimans, Ian Goodfellow, Wojciech Zaremba, Vicki Cheung, Alec Radford, and Xi Chen. Improved techniques for training GANs. In *Advances in Neural Information Processing Systems (NeurIPS)*, volume 29, pages 2234–2242, 2016. URL <https://proceedings.neurips.cc/paper/2016/hash/8a3363abe792db2d8761d6403605aeb7-Abstract.html>.
- [36] Yujia Li, Kevin Swersky, and Richard Zemel. Generative moment matching networks. In *Proceedings of the 32nd International Conference on Machine Learning (ICML)*, pages 1718–1727, 2015. URL <https://proceedings.mlr.press/v37/li15.html>.
- [37] Chun-Liang Li, Wei-Cheng Chang, Yu Cheng, Yiming Yang, and Barnabás Póczos. MMD GAN: Towards deeper understanding of moment matching network. In *Advances in Neural Information Processing Systems (NeurIPS)*, volume 30, pages 2203–2213, 2017. URL <https://proceedings.neurips.cc/paper/2017/hash/dfd7468ac613286cddb40872c8ef3b06-Abstract.html>.
- [38] Mingyang Deng, He Li, Tianhong Li, Yilun Du, and Kaiming He. Generative modeling via drifting. *arXiv preprint arXiv:2602.04770*, 2026. URL <https://arxiv.org/abs/2602.04770>.
- [39] Yousef Yeganeh, Azade Farshad, Ioannis Charisiadis, Marta Hasny, Martin Hartenberger, Björn Ommer, Nassir Navab, and Ehsan Adeli. Latent drifting in diffusion models for counterfactual medical image synthesis. In *Proceedings of the IEEE/CVF Conference on Computer Vision and Pattern Recognition (CVPR)*, pages 7685–7695, 2025. doi: 10.1109/CVPR52734.2025.00720.

- [40] Matthew Tancik, Pratul P. Srinivasan, Ben Mildenhall, Sara Fridovich-Keil, Nithin Raghavan, Utkarsh Singhal, Ravi Ramamoorthi, Jonathan T. Barron, and Ren Ng. Fourier features let networks learn high frequency functions in low dimensional domains. In *Advances in Neural Information Processing Systems (NeurIPS)*, volume 33, pages 7537–7547. Curran Associates, Inc., 2020. URL <https://arxiv.org/abs/2006.10739>.
- [41] Kyunghyun Cho, Bart van Merriënboer, Caglar Gulcehre, Dzmitry Bahdanau, Fethi Bougares, Holger Schwenk, and Yoshua Bengio. Learning phrase representations using RNN encoder–decoder for statistical machine translation. In *Proceedings of the 2014 Conference on Empirical Methods in Natural Language Processing (EMNLP)*, pages 1724–1734, Doha, Qatar, 2014. Association for Computational Linguistics. doi: 10.3115/v1/D14-1179. URL <https://aclanthology.org/D14-1179/>.
- [42] Zhou Wang, Eero P. Simoncelli, and Alan C. Bovik. Multiscale structural similarity for image quality assessment. In *The Thirty-Seventh Asilomar Conference on Signals, Systems and Computers, 2003*, volume 2, pages 1398–1402. IEEE, 2003. doi: 10.1109/ACSSC.2003.1292216.
- [43] Alexandros Karargyris, Renato Umeton, Micah J. Sheller, Alejandro Aristizabal, John George, Anna Wuest, Sarthak Pati, Hasan Kassem, Maximilian Zenk, Ujjwal Baid, Prakash Narayana Moorthy, Alexander Chowdhury, Junyi Guo, Sahil Nalawade, Jacob Rosenthal, David Kanter, Maria Xenochristou, Daniel J. Beutel, Verena Chung, Timothy Bergquist, James Eddy, Abubakar Abid, Lewis Tunstall, Omar Sanseviero, Dimitrios Dimitriadis, Yiming Qian, Xinxing Xu, Yong Liu, Rick Siow Mong Goh, Srini Bala, Victor Bittorf, Sreekar Reddy Puchala, Biagio Ricciuti, Soujanya Saineni, Eshna Sengupta, Akshay Chaudhari, Cody Coleman, Bala Desinghu, Gregory Damos, Debo Dutta, Diane Feddema, Grigori Fursin, Xinyuan Huang, Satyananda Kashyap, Nicholas Lane, Indranil Mallick, Pietro Mascagni, Virendra Mehta, Cassiano Ferro Moraes, Vivek Natarajan, Nikola Nikolov, Nicolas Padoy, Gennady Pekhimenko, Vijay Janapa Reddi, G. Anthony Reina, Pablo Ribalta, Abhishek Singh, Jayaraman J. Thiagarajan, Jacob Albrecht, Thomas Wolf, Geralyn Miller, Huazhu Fu, Prashant Shah, Daguang Xu, Poonam Yadav, David Talby, Mark M. Awad, Jeremy P. Howard, Michael Rosenthal, Luigi Marchionni, Massimo Loda, Jason M. Johnson, Spyridon Bakas, and Peter Mattson. Federated benchmarking of medical artificial intelligence with MedPerf. *Nature Machine Intelligence*, 5(7):799–810, 2023. doi: 10.1038/s42256-023-00652-2.
- [44] Ujjwal Baid, Satyam Ghodasara, Suyash Mohan, Michel Bilello, Evan Calabrese, Errol Colak, Keyvan Farahani, Jayashree Kalpathy-Cramer, Felipe C. Kitamura, Sarthak Pati, Luciano M. Prevedello, Jeffrey D. Rudie, Chiharu Sako, Russell T. Shinohara, Timothy Bergquist, Rong Chai, James Eddy, Julia Elliott, Walter Reade, Thomas Schaffter, Thomas Yu, Jiaxin Zheng, Ahmed W. Moawad, Luiz Otavio Coelho, Olivia McDonnell, Elka Miller, Fanny E. Moron, Mark C. Oswood, Robert Y. Shih, Loizos Siakallis, Yulia Bronstein, James R. Mason, Anthony F. Miller, Gagandeep Choudhary, Aanchal Agarwal, Cristina H. Besada, Jamal J. Derakhshan, Mariana C. Diogo, Daniel D. Do-Dai, Luciano Farage, John L. Go, Mohiuddin Hadi, Virginia B. Hill, Michael Iv, David Joyner, Christie Lincoln, Eyal Lotan, Asako Miyakoshi, Mariana Sanchez-Montano, Jaya Nath, Xuan V. Nguyen, Manal Nicolas-Jilwan, Johanna Ortiz Jimenez, Kerem Ozturk, Bojan D. Petrovic, Chintan Shah, Lubdha M. Shah, Manas Sharma, Onur Simsek, Achint K. Singh, Salil Soman, Volodymyr Statsevych, Brent D. Weinberg, Robert J. Young, Ichiro Ikuta, Amit K. Agarwal, Sword C. Cambren, Richard Silbergleit, Alexandru Dusoi, Alida A. Postma, Laurent Letourneau-Guillon, Gloria J. Guzman Perez-Carrillo, Atin Saha, Neetu Soni, Greg Zaharchuk, Vahe M. Zohrabian, Yingming Chen, Milos M. Cekic, Akm Rahman, Juan E. Small, Varun Sethi, Christos Davatzikos, John Mongan, Christopher Hess, Soonmee Cha, Javier Villanueva-Meyer, John B. Freymann, Justin S. Kirby, Benedikt Wiestler, Priscila Crivellaro, Rivka R. Colen, Aikaterini Kotrotsou, Daniel Marcus, Mikhail Milchenko, Arash Nazeri, Hassan Fathallah-Shaykh, Roland Wiest, Andras Jakab, Marc-Andre Weber, Abhishek Mahajan, Bjoern Menze, Adam E. Flanders, and Spyridon Bakas. The RSNA-ASNR-MICCAI BraTS 2021 benchmark on brain tumor segmentation and radiogenomic classification. *arXiv preprint arXiv:2107.02314*, 2021. URL <https://arxiv.org/abs/2107.02314>.
- [45] Bjoern H. Menze, Andras Jakab, Stefan Bauer, Jayashree Kalpathy-Cramer, Keyvan Farahani, Justin Kirby, Yuliya Burren, Nicole Porz, Johannes Slotboom, Roland Wiest, Levente Lenczi, Elizabeth Gerstner, Marc-Andre Weber, Tal Arbel, Brian B. Avants, Nicholas Ayache, Patricia

- Buendia, D. Louis Collins, Nicolas Cordier, Jason J. Corso, Antonio Criminisi, Tilak Das, Herve Delingette, Cagatay Demiralp, Christopher R. Durst, Michel Dojat, Senan Doyle, Joana Festa, Florence Forbes, Ezequiel Geremia, Ben Glocker, Polina Golland, Xiaotao Guo, Andac Hamamci, Khan M. Iftekharuddin, Raj Jena, Nigel M. John, Ender Konukoglu, Danial Lashkari, Jose Antonio Mariz, Raphael Meier, Sergio Pereira, Doina Precup, Stephen J. Price, Tammy Riklin Raviv, Syed M. S. Reza, Michael Ryan, Duygu Sarikaya, Lawrence Schwartz, Hoo-Chang Shin, Jamie Shotton, Carlos A. Silva, Nuno Sousa, Nagesh K. Subbanna, Gabor Szekely, Thomas J. Taylor, Owen M. Thomas, Nicholas J. Tustison, Gozde Unal, Flor Vasseur, Max Wintermark, Dong Hye Ye, Liang Zhao, Binsheng Zhao, Darko Zikic, Marcel Prastawa, Mauricio Reyes, and Koen Van Leemput. The multimodal brain tumor image segmentation benchmark (BRATS). *IEEE Transactions on Medical Imaging*, 34(10):1993–2024, 2015. doi: 10.1109/TMI.2014.2377694.
- [46] Spyridon Bakas, Hamed Akbari, Aristeidis Sotiras, Michel Bilello, Martin Rozycki, Justin S. Kirby, John B. Freymann, Keyvan Farahani, and Christos Davatzikos. Advancing the cancer genome atlas glioma MRI collections with expert segmentation labels and radiomic features. *Scientific Data*, 4(1):170117, 2017. doi: 10.1038/sdata.2017.117.
- [47] Spyridon Bakas, Hamed Akbari, Aristeidis Sotiras, Michel Bilello, Martin Rozycki, Justin Kirby, John Freymann, Keyvan Farahani, and Christos Davatzikos. Segmentation labels and radiomic features for the pre-operative scans of the TCGA-GBM collection, 2017.
- [48] Spyridon Bakas, Hamed Akbari, Aristeidis Sotiras, Michel Bilello, Martin Rozycki, Justin Kirby, John Freymann, Keyvan Farahani, and Christos Davatzikos. Segmentation labels and radiomic features for the pre-operative scans of the TCGA-LGG collection, 2017.
- [49] Sihong Chen, Kai Ma, and Yefeng Zheng. Med3D: Transfer learning for 3D medical image analysis. *arXiv preprint arXiv:1904.00625*, 2019. URL <https://arxiv.org/abs/1904.00625>.
- [50] Chaima Bensebihi, Nacer Eddine Benzebouchi, Nawel Zemmal, Abdallah Namoun, Aida Chefrour, and Siham Amrouch. An adaptive attention 3D U-Net for high-fidelity MRI-to-CT synthesis: Bridging the anatomical gap with CBAM. *Diagnostics*, 16(6):875, 2026. doi: 10.3390/diagnostics16060875.
- [51] Pareena Earwong, Chanon Puttanawarut, Sithiphong Suphaphong, Ladawan Worapruengkjaru, Chuleeporn Jarpinitnun, Thitipong Sawapabmongkon, Pimolpun Changkaew, Sawwanee Asavaphatiboon, and Suphalak Khachonkham. Clinical implementation of deep learning-based synthetic CT for MRI-only volumetric modulated arc therapy in head and neck and pelvic cancer patients. *Radiation Oncology*, 20(1):166, 2025. doi: 10.1186/s13014-025-02744-2.
- [52] Zhou Wang, Alan C. Bovik, Hamid R. Sheikh, and Eero P. Simoncelli. Image quality assessment: from error visibility to structural similarity. *IEEE Transactions on Image Processing*, 13(4): 600–612, 2004. doi: 10.1109/TIP.2003.819861.
- [53] Martin Heusel, Hubert Ramsauer, Thomas Unterthiner, Bernhard Nessler, and Sepp Hochreiter. GANs trained by a two time-scale update rule converge to a local Nash equilibrium. In *Advances in Neural Information Processing Systems (NeurIPS)*, 2017. URL <https://arxiv.org/abs/1706.08500>.
- [54] Tong-jie Yang, Peng-peng Wen, Xin Ye, Xiao-feng Wu, Cheng Zhang, Shi-yi Sun, Zi-xuan Wu, Guang-yi Zhang, Yi-fei Sun, Ren Ye, Cheng-kun Zhou, and Hai-jun He. CT hounsfield units in assessing bone and soft tissue quality in the proximal femur: A systematic review focusing on osteonecrosis and total hip arthroplasty. *PLOS ONE*, 20(3):e0319907, 2025. doi: 10.1371/journal.pone.0319907.
- [55] Samuel C. Leu, Zhibin Huang, and Ziwei Lin. Generation of pseudo-CT using high-degree polynomial regression on dual-contrast pelvic MRI data. *Scientific Reports*, 10(1):8118, 2020. doi: 10.1038/s41598-020-64842-3.
- [56] Chanwoong Lee, Young Hun Yoon, Jiwon Sung, Jun Won Kim, Yeona Cho, Jihun Kim, Jaehee Chun, and Jin Sung Kim. Abdominal synthetic CT generation for MR-only radiotherapy using structure-conserving loss and transformer-based cycle-GAN. *Frontiers in Oncology*, 14: 1478148, 2025. doi: 10.3389/fonc.2024.1478148.

A Qualitative comparisons

Figures 3–5 show axial, coronal, and sagittal reformats with baselines and error maps where applicable. Figures 6–7 show PCA projections of per-slice conditioning or context vectors.

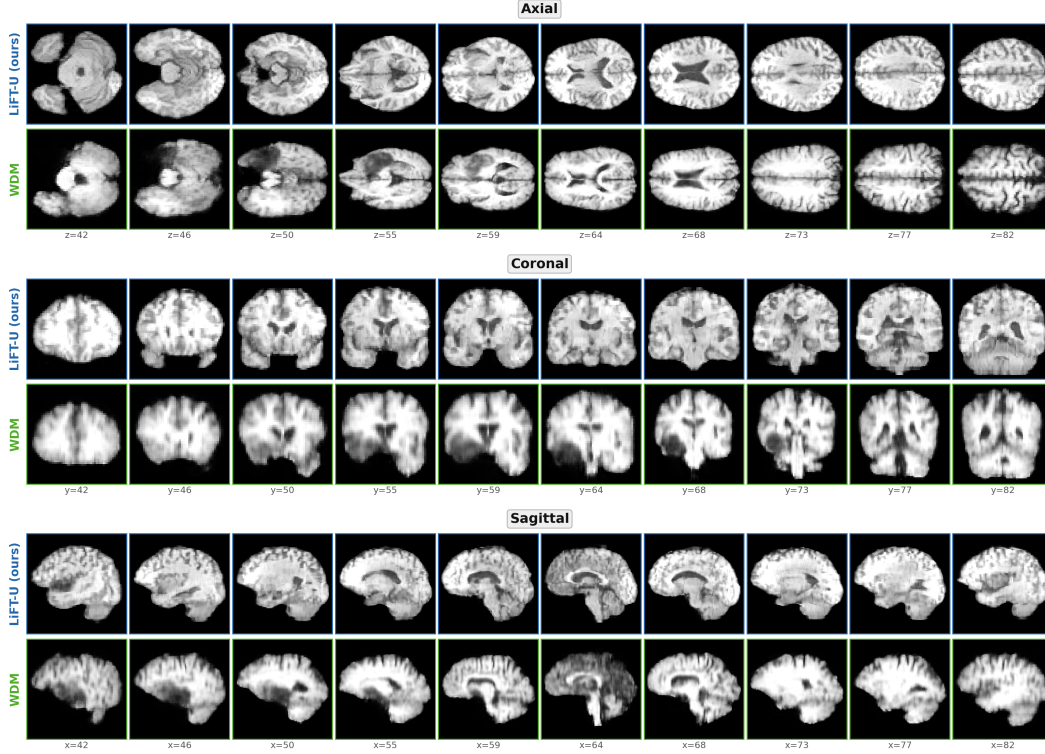


Figure 3: Qualitative reformats for unconditional brain MR generation: proposed LiFT-U (top of each block) versus WDM (bottom). Axial, coronal, and sagittal slices at ten depth indices each.

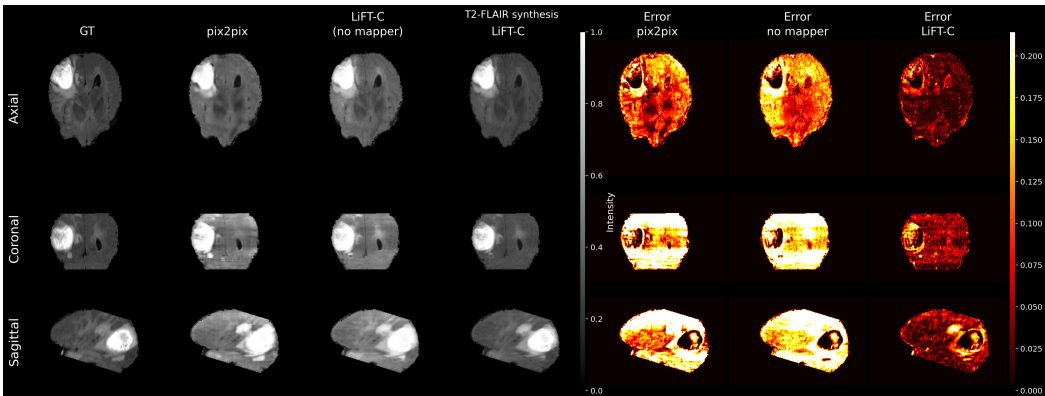


Figure 4: Qualitative reformats for missing-MR synthesis on BraTS 2023, T2-FLAIR target. Left block: ground truth (GT), pix2pix, LiFT-C without the z -context mixer, and full LiFT-C, shown in axial, coronal, and sagittal reformats. Right block: per-method absolute-error maps over the same volume.

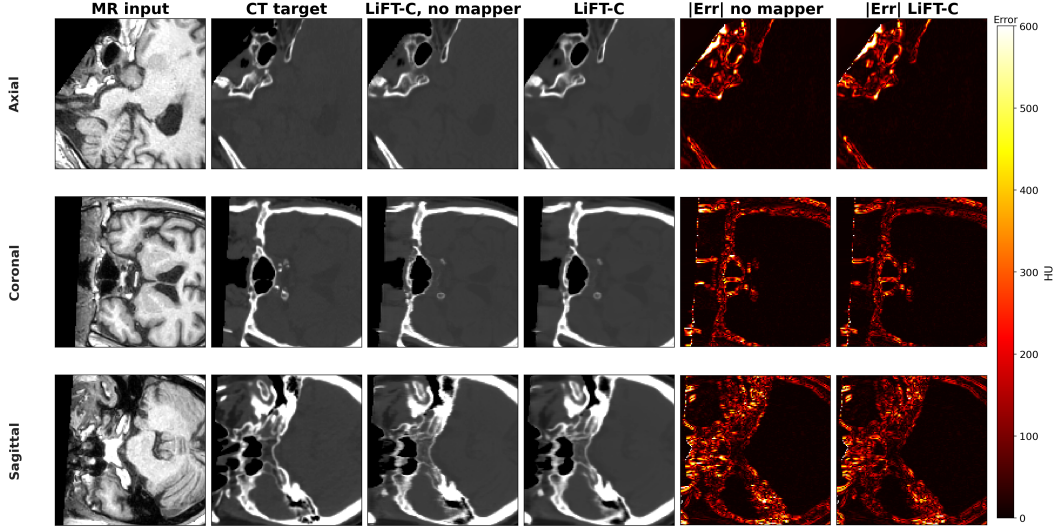


Figure 5: Qualitative reformats for MR-to-CT synthesis on SynthRAD2023, axial, coronal, and sagittal views. Columns: MR input, CT target, LiFT-C without the z -context mixer, full LiFT-C, and per-method absolute error maps in Hounsfield units.

Depth-trajectory visualization. For each task, we visualize the trajectory module’s outputs by stacking the per-slice conditioning vectors $c_{1:D}$ for several sample volumes and projecting them to two dimensions via PCA.

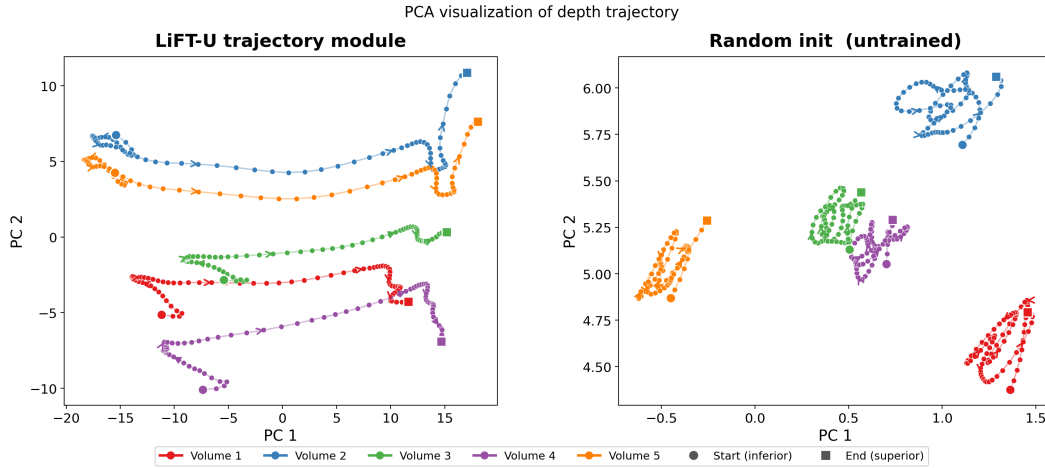


Figure 6: PCA projection of LiFT-U conditioning vectors for five generated volumes. Markers denote inferior (circle) and superior (square) endpoints of the slice sequence. The projected paths are visually ordered by slice index, consistent with depth-dependent conditioning by the trained mapper.

The projected trajectories vary with slice index in both Figures 6 and 7.

B Metric definitions

\hat{V} and V (or \hat{Y} and Y in the paired setting) denote predicted and reference volumes; N is the number of voxels in the relevant mask; Δ_z is the forward adjacent-slice difference operator $(\Delta_z V)_{i,j,k} = V_{i,j,k+1} - V_{i,j,k}$.

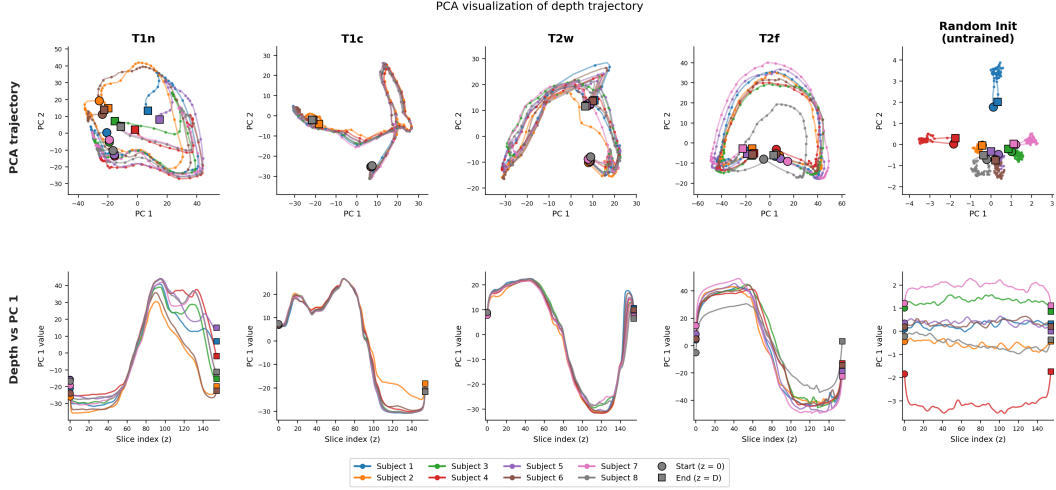


Figure 7: PCA projection of LiFT-C BiGRU context vectors for missing-MR synthesis. Top row: PC1–PC2 projections for each target contrast (T1n, T1c, T2w, T2f). Bottom row: PC1 as a function of slice index z for the eight displayed test subjects. Markers denote the first (circle) and last (square) slices. The projected context vectors vary smoothly with depth in these examples.

B.1 Image-similarity metrics

MAE. Voxel-wise mean absolute error,

$$\text{MAE}(\hat{Y}, Y) = \frac{1}{N} \sum_v |\hat{Y}_v - Y_v|.$$

Reported in Hounsfield units (HU) for CT and in normalized intensity for MR.

RMSE. Root mean squared error, $\text{RMSE} = \sqrt{(1/N) \sum_v (\hat{Y}_v - Y_v)^2}$.

PSNR. Peak signal-to-noise ratio,

$$\text{PSNR}(\hat{Y}, Y) = 20 \log_{10} \left(\frac{\text{MAX}}{\text{RMSE}(\hat{Y}, Y)} \right),$$

where MAX is the dynamic range of the target signal (e.g., the post-clipping CT range or the $[0, 1]$ MR range).

SSIM. Structural similarity index [52], computed as a 3D Gaussian-weighted SSIM with window size 11 and $\sigma = 1.5$ unless otherwise noted. Per-orientation reformat SSIMs (axial, coronal, sagittal) are 2D SSIMs computed slice-by-slice in each plane and averaged.

NCC. Normalized cross-correlation between voxel intensities (Pearson correlation over the body mask).

FID. Fréchet inception distance [53] between deep-feature distributions of generated and real volumes,

$$\text{FID} = \|\mu_g - \mu_r\|_2^2 + \text{tr}(\Sigma_g + \Sigma_r - 2(\Sigma_g \Sigma_r)^{1/2}),$$

where (μ, Σ) are the mean and covariance of the deep features. For Task A, features are 2048-dimensional MedicalNet ResNet-50 activations [49] computed on 1,000 generated and 1,000 real volumes following the WDM protocol [12].

B.2 Through-plane coherence metrics

Δ_z MAE. Adjacent-slice derivative MAE,

$$\Delta_z \text{MAE}(\hat{Y}, Y) = \frac{1}{N_\Delta} \sum_v |(\Delta_z \hat{Y})_v - (\Delta_z Y)_v|,$$

averaged over the relevant region mask. This metric quantifies the difference between predicted and reference adjacent-slice intensity changes. Region-restricted variants (Bone, Air, Boundary) restrict the sum to voxels in the corresponding mask.

Δ_z correlation. Pearson correlation between $\text{vec}(\Delta_z \hat{Y})$ and $\text{vec}(\Delta_z Y)$ over the body mask. This metric measures linear agreement between predicted and reference adjacent-slice differences, complementing voxel-wise MAE.

B.3 Reformat / plane-wise metrics (Task B)

Reformat SSIM. 2D SSIM (window 11, $\sigma = 1.5$) computed in each orthogonal plane (axial, coronal, sagittal) and averaged across slices in that plane.

B.4 Statistical reporting

Bootstrap 95% CI. Subject-level bootstrap with 10,000 resamples drawn with replacement from the test cohort. We report the empirical 2.5 and 97.5 percentiles of the resampled mean as [low, high].

Paired Wilcoxon signed-rank test. Two-sided paired test on per-subject metric values (LiFT-C vs. baseline or vs. no-mapper) on a fixed test split. Significance encoding throughout the appendix tables: *** for $p < 0.0001$, * for $p < 0.05$.

B.5 Region masks (CT)

For CT-domain evaluation in Task C, region masks are derived from the reference CT to avoid prediction-dependent masking. Soft tissue is defined as $-100 \leq \text{HU} \leq 200$ (the standard radiological soft-tissue window), bone as $\text{HU} > 300$, and air as $\text{HU} < -500$, consistent with canonical HU anchors in which air sits near -1000 HU, water at 0 HU, and bone occupies the upper several hundred HU [54]. The boundary mask is a 2-voxel dilation of the $\text{bone} \cup \text{air}$ union, intended to isolate high-gradient air-tissue and soft-tissue-bone interfaces that are challenging for MR-to-CT synthesis [27]; explicit interface regions of comparable scale (2–3 mm margin around bone) have been used in prior pseudo-CT work [55]. The body mask is the largest connected component of $\text{HU} > -500$ with internal holes filled, following CT-based largest-connected-component preprocessing used in MR-to-sCT pipelines [56]. CT volumes are clipped to $[-1000, 2000]$ HU prior to evaluation.

B.6 Resource metrics

Inference memory (GB). Peak GPU memory measured during a single forward pass that synthesizes one volume at the listed resolution.

Inference time per volume (s). Wall-clock time per volume on a single NVIDIA RTX 5090, forward inference only (excluding data loading and preprocessing). For Task B (missing-MR), the LiFT-C and pix2pix per-volume times in Table 2 are averaged over 1,000 generated volumes; cWDM timing is measured with the official open-source repository (1000-step DDPM sampler) and reports the forward-only synthesis cost of one native-resolution volume.

C Missing-MR statistical analysis

For LiFT-C and pix2pix, we report bootstrap 95% confidence intervals (10,000 resamples across the 219 subjects) and paired Wilcoxon signed-rank p -values. cWDM is listed as an aggregate point estimate from the original paper; per-subject cWDM scores were unavailable.

Table 5: Missing-MR PSNR (dB, \uparrow): LiFT-C and pix2pix mean with 95% bootstrap CI; published cWDM aggregate point estimate from [13]. Paired Wilcoxon signed-rank two-sided p -values for LiFT-C versus pix2pix are $p < 0.001$ for every contrast and for the average.

Contrast	LiFT-C	pix2pix	Published cWDM [13]
T1n	29.42 [29.00, 29.84]	27.61 [27.30, 27.92]	29.74
T1c	27.40 [27.00, 27.81]	25.91 [25.56, 26.25]	27.32
T2w	28.53 [28.05, 28.98]	26.69 [26.29, 27.07]	28.81
T2f	27.88 [27.51, 28.23]	25.19 [24.91, 25.47]	27.83
Avg.	28.31 [28.02, 28.59]	26.35 [26.12, 26.57]	28.42

Table 6: Missing-MR 3D-Gaussian SSIM (\uparrow): LiFT-C and pix2pix mean with 95% bootstrap CI; published cWDM aggregate point estimate from [13]. Paired Wilcoxon signed-rank two-sided p -values for LiFT-C versus pix2pix are $p < 0.001$ for every contrast and for the average.

Contrast	LiFT-C	pix2pix	Published cWDM [13]
T1n	0.9615 [0.9594, 0.9636]	0.9475 [0.9455, 0.9494]	0.9622
T1c	0.9460 [0.9435, 0.9484]	0.9316 [0.9294, 0.9339]	0.9451
T2w	0.9571 [0.9541, 0.9599]	0.9419 [0.9392, 0.9445]	0.9588
T2f	0.9424 [0.9400, 0.9449]	0.9169 [0.9146, 0.9192]	0.9438
Avg.	0.9518 [0.9497, 0.9538]	0.9345 [0.9325, 0.9363]	0.9525

Table 7: LiFT-C plane-wise SSIM on missing-MR ($N = 219$ validation). SSIM [52] is the mean 2D SSIM in each orthogonal plane.

Contrast	SSIM _{ax} \uparrow	SSIM _{cor} \uparrow	SSIM _{sag} \uparrow
T1n	0.9608	0.9592	0.9575
T1c	0.9490	0.9456	0.9447
T2w	0.9571	0.9556	0.9548
T2f	0.9418	0.9418	0.9395
Avg.	0.9522	0.9505	0.9491

Paired ablation statistics (MR-to-CT). For the MR-to-CT ablation, we compared LiFT-C with the no-mapper Stage-1 baseline on the same 36-subject test split using two-sided paired Wilcoxon signed-rank tests. The improvements in the primary image-domain metrics reported in Table 3 were significant ($p < 10^{-4}$ for MAE, PSNR, SSIM, and NCC). The through-plane metrics in Table 4 showed the same pattern ($p < 10^{-4}$ for full-volume Δ_z MAE, bone Δ_z MAE, air Δ_z MAE, and Δ_z correlation). Region-wise MAE tests were also significant for soft tissue, bone, and boundary regions ($p < 10^{-4}$), while air-region MAE was weaker ($p = 0.041$). These p -values are nominal and are reported only to support the paired ablation, not to establish clinical superiority.

Extended MR-to-CT comparison. Tables 8 and 9 report supplementary Δ_z MAE breakdowns and per-orientation reformat SSIM across the five MR-to-CT methods. Bolded entries indicate the best per-column value.

D Memorization probe

We evaluate exact-copying risk using nearest-neighbor retrieval from generated or predicted volumes to the training set. For each task, we compare the LiFT query set against a held-out real-volume baseline under a task-appropriate distance metric. These results should be interpreted only as exact-copying diagnostics; they do not rule out membership inference, attribute inference, or other forms of privacy leakage.

Table 8: MR-to-CT supplementary through-plane metrics on the 36-subject test set: per-region Δ_z MAE (HU, \downarrow) for body, soft tissue, and the dilated bone \cup air boundary. Bold marks the best per column.

Method	Δ_z MAE Body \downarrow	Δ_z MAE Soft \downarrow	Δ_z MAE Bdry \downarrow
Pix2pix-UNet	49.15	18.59	168.01
Pix2pix-ResNet	41.79	14.45	147.65
CBAM3D-UNet	37.38	13.34	130.53
LiFT-C, no mapper	40.00	14.01	140.39
LiFT-C	35.87	12.71	125.09

Table 9: MR-to-CT per-orientation reformat SSIM on the 36-subject test set. SSIM is computed in each orthogonal plane. Bold marks the best per column.

Method	SSIM Axial \uparrow	SSIM Coronal \uparrow	SSIM Sagittal \uparrow
Pix2pix-UNet	0.803	0.807	0.807
Pix2pix-ResNet	0.856	0.861	0.860
CBAM3D-UNet	0.842	0.848	0.849
LiFT-C, no mapper	0.861	0.865	0.865
LiFT-C	0.867	0.872	0.872

Across the three nearest-neighbor probes, we find no evidence of exact copying. For unconditional MRI, LiFT-U samples are farther from the training set than held-out real volumes: the generated-to-train nearest-neighbor MAE is 0.063 ± 0.007 in $[-1, 1]$ -normalized MR space, compared with 0.026 ± 0.004 for held-out real volumes. The closest LiFT-U–training pair has MAE 0.052, above the closest held-out real–training pair (0.020); WDM samples under the same probe yield 0.073 ± 0.007 .

For missing-MR synthesis, LiFT-C predictions are on average $1.26\times$ farther from the training set than training subjects are from each other under the pooled-descriptor MSE probe (per-contrast ratios T1n 1.053, T1c 1.675, T2w 1.155, T2f 1.162). The corresponding GT-validation ratio is 1.088, consistent with disjoint validation and training splits drawn from the same distribution.

For MR-to-CT, LiFT-C predictions are slightly closer to the training CT set than GT test volumes (165.8 ± 23.9 HU versus 172.7 ± 26.2 HU), but the closest LiFT-C–training pair remains 118.8 HU away, comparable to the closest GT-test–training pair (126.6 HU). No prediction has near-zero nearest-neighbor error under full-volume HU L1 distance. The reversed direction relative to Tasks A and B is consistent with regression-style supervised translation: per-voxel MR-to-CT prediction acts as a conditional-mean estimator and produces smoother volumes than independently sampled real CTs, so mean distance to the training set drops without indicating duplication. The closest-pair distance, which is the relevant exact-copy diagnostic, remains in the same range as the held-out GT-test–training pair.

Task A: LiFT-U unconditional MRI. We sample $n = 200$ generated volumes ($T = 1.25$, $\sigma_z = 1.5$, seed 15213) and compute the voxel-wise L1 distance from each generated volume to its nearest training-set neighbor in $[-1, 1]$ -normalized MR space. The held-out 219-subject evaluation cohort serves as the real-volume baseline.

Task B: LiFT-C missing-MR. For each predicted validation volume, we compute the nearest training-set neighbor using MSE on $16 \times 16 \times 8$ average-pooled descriptors (2048 voxels). The reference is the average train–train pairwise distance; a ratio above 1 indicates that predictions are farther from training subjects than training subjects are from each other.

Task C: LiFT-C MR-to-CT. For each of the 36 test predictions, we compute full-volume L1 distance in HU to the nearest of the 144 training CTs. This probe is intentionally conservative: it tests for near-duplicate CT outputs, not for membership inference or other privacy leakage.

E Datasets and licenses

We used only publicly released datasets and pretrained weights. No new patient data were collected, and no derived dataset is released with this work.

BraTS 2023 GLI (Tasks A and B). We use the BraTS 2023 GLI (Adult Glioma) cohort from the RSNA-ASNR-MICCAI Brain Tumor Segmentation Challenge, distributed via the Synapse portal under a data-use agreement that permits academic, non-commercial research use and requires citation of the BraTS challenge papers. Subject MRIs in this release are de-identified and skull-stripped by the challenge organizers; no additional human-subject data was collected for this paper.

SynthRAD2023 Task 1 – Brain (Task C). We use the SynthRAD2023 Task 1 (Brain) MR-CT pairs released through the SynthRAD challenge organizers [27], used under the terms of the public challenge release for non-commercial research. Co-registration and de-identification are provided by the challenge organizers; we use a patient-level 80/20 train/test split of the 180 public subjects (144 train / 36 test).

MedicalNet ResNet-50 (FID feature extractor). The 3D MedicalNet ResNet-50 weights [49] used to compute FID for Task A are released by Tencent on GitHub under the MIT license. We use them strictly as a frozen feature extractor for evaluation; no fine-tuning is performed.

Baseline reference implementations. The pix2pix baseline [24] is reproduced by us under our shared evaluation pipeline using the official open-source repository under its permissive open-source license. For cWDM [13], we use the official open-source repository under its permissive open-source license only for runtime measurement (Table 2); reconstruction-quality numbers are taken from the original paper.

F Training hyperparameters

All experiments were trained on a single NVIDIA RTX 5090 GPU. Table 10 summarizes the main training settings. Additional implementation-level defaults, including optimizer betas, EMA decay, augmentation flags, gradient clipping, warmup, and checkpointing details, will be released with the code.

Table 10: Main training settings for LiFT experiments. Differential learning rates are listed as U-Net / BiGRU.

Task	Trainable module	Optimizer / LR	Batch construction
LiFT-U Stage 1	2D axial generator	Adam, 2×10^{-4}	128 axial slices
LiFT-U Stage 2	depth mapper	Adam, 2×10^{-4}	8 volumes
Missing-MR LiFT-C	2D U-Net + BiGRU	AdamW, $2 \times 10^{-5} / 2 \times 10^{-4}$	1 volume; 48 decoded slices
MR-to-CT Stage 1	2D U-Net	Adam, 2×10^{-4}	32 axial slices
MR-to-CT Stage 2	BiGRU + residual head	AdamW, 2×10^{-4}	32 three-slice windows

For LiFT-U, the frozen feature extractor for tri-planar drift is an ImageNet-pretrained ResNet-18, and inference uses sampling temperature $T = 1.25$. For missing-MR, the BiGRU processes all $D = 155$ slice descriptors before decoding the sampled training slices. For MR-to-CT, Stage 2 is trained on top of the frozen Stage 1 translator and predicts an additive residual correction; the BiGRU likewise processes all $D = 128$ slice descriptors per volume, while “three-slice windows” refers to the decoded slices supervised at each training step (the full-depth context is preserved on the encoder side). During training, each term of Eq. (9) is estimated on the decoded slice subset at each step (48 contiguous slices for Missing-MR; 32 three-slice windows for MR-to-CT Stage 2), while the full-depth encoder context is preserved. Best checkpoints are selected by validation MAE on a held-out training-set fold for MR-to-CT and by validation reconstruction/generation metrics on the BraTS validation split for Tasks A and B.

G Algorithms

Algorithm 1 LiFT-U Stage-2 training step. The real feature bank \mathcal{B}_π from Eq. (4) is approximated per minibatch by the real features $\mathcal{F}_{\text{real}}^\pi$ of the B sampled volumes; this is the empirical estimator used during training.

Require: minibatch latents $\{z_i\}_{i=1}^B$, real volumes $\{V_j\}_{j=1}^B$, frozen 2D generator $G_{2D}(\cdot; \theta)$, depth mapper M_ϕ , frozen feature extractor E_{feat} , learning rate α

Ensure: updated mapper parameters ϕ

```

1: for  $i = 1, \dots, B$  do                                ▷ generate synthetic volume from latent  $z_i$ 
2:   for  $d = 1, \dots, D$  do
3:      $c_{i,d} \leftarrow M_\phi(z_i, \gamma(d))$ 
4:      $\hat{v}_{i,d} \leftarrow G_{2D}(c_{i,d}; \theta)$ 
5:   end for
6:    $\hat{V}_i \leftarrow \text{Stack}_{d=1}^D \hat{v}_{i,d}$ 
7: end for
8:  $\mathcal{L}_{\text{LiFT-U}} \leftarrow 0$ 
9: for  $\pi \in \{\pi_{xy}, \pi_{yz}, \pi_{xz}\}$  do                    ▷ tri-planar feature distributions
10:   $\mathcal{F}_{\text{gen}}^\pi \leftarrow \{E_{\text{feat}}(\pi(\hat{V}_i))\}_{i=1}^B$ 
11:   $\mathcal{F}_{\text{real}}^\pi \leftarrow \{E_{\text{feat}}(\pi(V_j))\}_{j=1}^B$ 
12:   $\mathcal{L}_{\text{LiFT-U}} \leftarrow \mathcal{L}_{\text{LiFT-U}} + \text{Drift}(\mathcal{F}_{\text{gen}}^\pi, \mathcal{F}_{\text{real}}^\pi)$ 
13: end for
14:  $\phi \leftarrow \phi - \alpha \cdot \nabla_\phi \mathcal{L}_{\text{LiFT-U}}$ 

```

Algorithm 2 LiFT-C two-pass native-resolution inference

Require: source volume $X \in \mathbb{R}^{C_{\text{in}} \times H \times W \times D}$, encoder E_θ , decoder D_θ , z -mixer M_{ϕ_C}

Ensure: synthesized target volume \hat{Y}

```

1: for  $d = 1, \dots, D$  do                                ▷ Pass 1: encode every slice, retain only pooled bottleneck
2:    $h_d \leftarrow E_\theta(X_d)$                                 ▷ forward pass; skip activations discarded to reduce memory
3:    $b_d \leftarrow \text{Pool}(h_d)$ 
4: end for
5:  $(c_1, \dots, c_D) \leftarrow M_{\phi_C}(b_{1:D}, \gamma(1:D))$     ▷ bidirectional GRU produces depth-context vectors
6: for  $d = 1, \dots, D$  do                                ▷ Pass 2: re-encode and decode with context
7:    $h_d \leftarrow E_\theta(X_d)$                                 ▷ re-encode to recover skip connections
8:    $\hat{y}_d \leftarrow D_\theta(h_d, c_d)$ 
9: end for
10:  $\hat{Y} \leftarrow \text{Stack}_{d=1}^D \hat{y}_d$ 

```
